Journal of Biomolecular NMR, **17:** 215–230, 2000.
KLUWER/ESCOM

Backbone dynamics and solution structure refinement of the ^{15}N-labeled human oncogenic protein p13^{MTCP1}: Comparison with X-ray data

Laurent Guignard[a], André Padilla[a], Joel Mispelter[b], Yin-Shan Yang[a], Marc-Henri Stern[c], Jean-Marc Lhoste[a] & Christian Roumestand[a,*]

[a]*Centre de Biochimie Structurale, CNRS-UMR 9955, INSERM-U414, Université de Montpellier I, Faculté de Pharmacie, 15 Avenue Charles Flahault, F-34060 Montpellier Cedex, France;* [b]*Unité INSERM U350, Institut Curie, Biologie, Centre Universitaire Bât 112, F-91405 Orsay Cedex, France;* [c]*Unité INSERM U462, Hôpital Saint-Louis, F-75475 Paris, France*

Received 20 December 1999; Accepted 24 April 2000

Key words: leukemia, NMR structure, protein dynamics, translocations

Abstract

Two related oncogenes, *TCL1* and *MTCP1*, are overexpressed in certain T-cell prolymphocytic leukemias as a result of chromosomal rearrangements that involve the translocation of one T-cell receptor gene to either chromosome 14q32 or Xq28, respectively. The human oncoprotein p13^{MTCP1} is coded by the *MTCP1* gene and its primary sequence is highly and only homologous to that of p14^{TCL1}, the product of *TCL1*. These two proteins likely represent the first members of a new family of oncogenic proteins. A previous model of the three-dimensional solution structure of p13^{MTCP1} was determined recently using exclusively homonuclear proton two-dimensional NMR methods and, almost simultaneously, high-resolution crystal structures of p13^{MTCP1} and p14^{TCL1} appeared in the literature. In order to gain more insight into the details of the solution structure, we uniformly labeled p13^{MTCP1} with nitrogen-15. The refined structure benefits from 520 additional NOEs, extracted from either ^{15}N-edited 3D experiments or homonuclear 2D NOESY recorded at 800 MHz, and from a nearly complete set of ϕ angular restraints. Measurements of ^{15}N spin relaxation times and heteronuclear ^{15}N{^{1}H}NOEs at two magnetic field strengths provided additional insights into the dynamics of the protein backbone. On the basis of these new results, a putative binding surface for this particular class of oncogenes is discussed.

Abbreviations: 2D (3D), two-dimensional (three-dimensional); NOE, nuclear Overhauser enhancement; ^{15}N{^{1}H} NOE, heteronuclear ^{15}N nuclear Overhauser enhancement; NOESY, nuclear Overhauser enhancement spectroscopy; DQF-COSY, double-quantum-filtered scalar-correlated spectroscopy; *z*-TOCSY, *z*-filtered total correlation spectroscopy; HSQC, heteronuclear single quantum coherence; $R_N(N_z)$ (R_1), heteronuclear ^{15}N longitudinal relaxation rate; $R_N(N_{xy})$ (R_2), heteronuclear ^{15}N longitudinal relaxation rate; $R_N(H_z \rightarrow N_z)$, cross-relaxation rate between ^{15}N and its attached amide proton; rmsd, root mean square deviation; PCR, polymerase chain reaction.

Introduction

T-cell lymphoproliferative diseases are often associated with recurrent chromosomal translocations involving T-cell receptor genes (TCR) and genes that are thought to play a role in the pathogenesis of these diseases (Croce, 1987). These chromosomal translocations have been proposed to occur during recombination events of the TCR genes: they juxtapose cellular protooncogenes to enhancer elements, leading to deregulation of oncogene expression. The two oncogenes often involved in these translocations are *MTCP1* (also called *c6.1B*) (Fisch et al., 1993; Stern et al., 1993) and *TCL1* (Virgilio et al., 1993; Fu et al., 1994; Narducci et al., 1995; Thick et al., 1996), which

*To whom correspondence should be addressed. E-mail: roume@cbs.univ-montp1.fr

belong to a new family of genes involved in lymphoid proliferation and T-cell malignancies. Very recently, a new gene named *TCL1b* (Pekarsky et al., 1999) has been identified, located ≈16 kb centromeric of *TCL1*. It is also involved in similar T-cell leukemias and constitutes the third gene identified from this new family.

The *MTCP1* gene, located in the Xq28 chromosomal region, was the first gene to be identified in the heterogenous group of uncommon T-cell leukemias presenting a mature phenotype (Stern et al., 1993). It is involved in the translocation t(X;14)(q28;q11), a translocation recurrently associated with this type of T-cell proliferations. It codes for a 107-residue (13 kDa) protein known as p13^{MTCP1} (Madani et al., 1996), which expression is restricted to mature T-cell proliferations with t(X;14) translocations (Madani et al., 1995). This protein shows high sequence homology (40% identity, 61% similarity) with p14^{TCL1} (Fu et al., 1994), the product of the 14q32.1 oncogene *TCL1*, and with p14^{TCL1b} (36% identity, 63% similarity), the product of the newly identified *TCL-1b* oncogene (Pekarsky et al., 1999).

We reported previously the elucidation of the 3D structure of p13^{MTCP1} using exclusively homonuclear 2D NMR (Yang et al., 1998). Then, using this previous model of the solution structure of p13^{MTCP1} for molecular replacement, the crystal structure of p14^{TCL1} was solved in our laboratory (Hoh et al., 1998). Finally, a high resolution crystal structure of p13^{MTCP1} was determined using multiwavelength anomalous dispersion data from selenomethionine-enriched protein (Fu et al., 1998). The two oncogenic proteins p13^{MTCP1} and p14^{TCL1} share a virtually identical 3D structure, the main structural motif of which consists of a compact eight-stranded β-barrel with an original topology. Interestingly, p13^{MTCP1} is a monomeric protein, whereas p14^{TCL1} forms a tight dimer both in the crystal and in solution, as indicated by gel filtration and DOSY experiments (unpublished results). Structural similarities between p14^{TCL1} and p13^{MTCP1} suggest that their (unknown) function may be analogous and allow their classification as a novel class of oncogenes. In the present paper, we now report the refined solution structure of the ^{15}N-labeled protein p13^{MTCP1}, using double-resonance heteronuclear NMR. We complemented the structural study by an analysis of the backbone dynamics using experimental ^{15}N relaxation parameters measured on the NH vectors at two magnetic field strengths. Implications for the cellular function of these oncogene products are discussed on the basis of a comparison of both structural and dynamical features of the solution and the crystal structure of p13^{MTCP1}.

Materials and methods

Protein preparation

A more precise cloning of the p13^{MTCP1} gene was done, using PCR-based mutagenesis, in order to eliminate the eight extra residues introduced at the C-terminal end of the protein expressed in our original pGEX- p13^{MTCP1} construct. The resulting pGEX-p13^{MTCP1} was introduced into *E. coli* strain BL21. The mutant protein was purified as previously described for the original construct (Yang et al., 1998). Uniform ^{15}N labeling was achieved by growing the cells in minimal medium with $^{15}NH_4Cl$ as sole nitrogen source.

NMR measurements

NMR experiments were carried out at 9.4 or 14.1 Tesla on Bruker AMX400 and AMX600 spectrometers equipped with 5 mm *z*-gradient ^{1}H-^{13}C-^{15}N triple resonance probes. Protein samples were dissolved in a 20 mM phosphate buffer with 10% $^{2}H_2O$ for the lock. The pH was adjusted to 6.5 and the temperature set to 30 °C. In all experiments, the ^{1}H carrier was centred on the water resonance and a WATERGATE (Piotto et al., 1992; Sklenar, 1995) sequence was incorporated to suppress the solvent resonance. Quadrature detection in the indirect dimensions was achieved using States-TPPI (Marion et al., 1989b). In addition, 2D homonuclear experiments were performed at 800 MHz (Bruker DMX800) on a non-enriched protein sample dissolved in heavy water. NMR spectra were processed with the Gifa (version 4.22; Pons et al., 1996) software utility.

2D homonuclear spectroscopy

Homonuclear 2D experiments (NOESY (Jeener et al., 1979), *z*-TOCSY (Rance, 1987) and DQF-COSY (Rance et al., 1983)) were carried out at 800 MHz on a 1 mM non-enriched protein sample using similar experimental conditions and parameters as previously described (Yang et al., 1998).

$^{3}J_{NH-H\alpha}$ measurement

A series of 12 J-modulated [^{1}H,^{15}N] COSY spectra (Neri et al., 1990) was performed at 600 MHz on a

1 mM ^{15}N-labeled protein sample, using different evolution delays in the range 10–100 ms for homonuclear J-modulation. The conventional experiment was modified in order to introduce the WATERGATE sequence in the last reverse INEPT step for water suppression purposes (Santoro et al., 1996). The peak heights were then fitted accordingly (Billeter et al., 1992) to extract the individual coupling constant values.

[^{1}H,^{15}N] 3D experiments

NOESY-HSQC and TOCSY-HSQC (Fesik and Zuiderweg, 1988; Marion et al., 1989a; Bax et al., 1990) double resonance [^{1}H,^{15}N] 3D spectra were acquired at 600 MHz with a uniformly ^{15}N-labeled 2 mM sample of protein. The NOESY experiments were recorded with a mixing time of 150 ms and the TOCSY experiment with an isotropic mixing period (TOWNY (Kadkhodaei et al., 1993)) of 60 ms. WALTZ-16 modulation (Shaka et al., 1983) was used to decouple ^{15}N during acquisition.

Relaxation rate constant and ^{15}N{^{1}H}NOE measurements

Relaxation rate constant measurements were performed on a 1 mM protein sample, at 9.4 T (400 MHz) and 14.1 T (600 MHz). The pulse sequences used to determine ^{15}N $R_N(N_z)$ (R_1), $R_N(N_{xy})$ (R_2), and ^{15}N{^{1}H}NOE values were similar to those described (Kay et al., 1992; Peng and Wagner, 1992a,b), experimental parameters and processing were similar to those previously reported for the relaxation study of C12A-p8^{MTCP1} (Barthe et al., 1999).

Molecular modeling calculations

All calculations were carried out following the standard protocol described for our previous model of p13^{MTCP1} (Yang et al., 1998). Briefly, distance restraints were obtained from the volume of cross peaks measured on 2D NOESY and [^{1}H-^{15}N] 3D NOESY-HSQC spectra and classified as strong, medium and weak corresponding to 2.4, 3.6 and 4.8 Å upper bounds. Angular restraints on the ϕ dihedral angles were obtained from the coupling constants $^3J_{NH-H\alpha}$, using two cutoffs for coupling constants greater than 8.0 Hz and less than 6.0 Hz, respectively constrained to $-120°\pm30°$ and $-90°\pm30°$. In addition, χ_1 angles were obtained from the analysis of the $^3J_{H\alpha-H\beta}$ coupling constants and intra-residue NOEs (Hyberts et al., 1987). From these restraints, a set of 20 structures was generated with the variable target function program DYANA (Güntert et al., 1997), using the torsion angle dynamic algorithm, with a value of the target function smaller than 3 Å^2 and no distance violation larger than 0.3 Å. The ϕ and χ_1 angles showed no violation greater than 5°. The average structure obtained from the 20 best structures (based on the final target penalty function values) was further refined with molecular mechanics energy with the SANDER module of AMBER 4.1 (Pearlman et al., 1995) using the 1994 force field (Cornell et al., 1995).

Relaxation data analysis

When the relaxation of the ^{15}N nucleus is predominantly caused by the dipolar interaction with its attached amide proton and by the anisotropy of its chemical shift, the relaxation data can be interpreted in terms of the motion of the ^{15}N-^{1}H vector. Given that the three experimentally determined parameters, $R_N(N_z)$, $R_N(N_{xy})$ and NOE, depend on the spectral density function at five different frequencies (Abragam, 1961), the calculation of the spectral density values can be approached by the application of the so-called reduced spectral density mapping, in which the relaxation rates are directly translated into spectral density at three different frequencies (Peng and Wagner, 1992a,b; Farrow et al., 1995; Ishima and Nagayama, 1995a,b; Lefèvre et al., 1996):

$$\begin{bmatrix} J(0) \\ J(\omega_N) \\ < J(\omega_H) > \end{bmatrix} = \begin{bmatrix} \frac{-3}{4(3d^2+c^2)} & \frac{3}{2(3d^2+c^2)} & \frac{-9}{10(3d^2+c^2)} \\ \frac{1}{(3d^2+c^2)} & 0 & \frac{-7}{5(3d^2+c^2)} \\ 0 & 0 & \frac{1}{5d^2} \end{bmatrix} \times \begin{bmatrix} R_N(N_z) \\ R_N(N_{x,y}) \\ R_N(H_z \rightarrow N_z) \end{bmatrix} \quad (1)$$

in which

$$d^2 = (\frac{\mu_0}{4\pi})^2 \frac{h^2\gamma_N^2\gamma_H^2}{(4\pi)^2 r_{NH}^6} \text{ and}$$

$$c^2 = \frac{1}{3}(\gamma_N B_0)^2(\Delta\sigma)^2$$

where μ_0 is the permeability of vacuum, *h* is Planck's constant, γ_H (2.6752 10^8 rad.s^{-1}.T^{-1}) and

γ_N ($-2.711\ 10^7$ rad.s^{-1}.T^{-1}) are the gyromagnetic ratios of the ^{1}H and the ^{15}N nuclei, respectively, and ω_H and ω_N are the ^{1}H and ^{15}N Larmor frequency, respectively; r_{NH} is the internuclear ^{15}N-^{1}H distance (1.02 Å), B_0 is the magnetic field strength, and $\Delta\sigma$ is the difference between the parallel and perpendicular components of the axially symmetric ^{15}N chemical shift tensor, estimated to be -160 ppm (Hiyama et al., 1988). For a magnetic field of 14.1 (9.4) Tesla, $d^2 = 1.2986\ 10^9$ rad^2.s^{-2} and $c^2 = 1.2452\ 10^9$ ($0.553\ 10^9$) rad^2.s^{-2}. The cross-relaxation rate $R_N(H_z \rightarrow N_z)$ between ^{15}N and its attached amide proton is correlated with NOE and is calculated using $NOE = 1 + (\gamma_H/\gamma_N).R_N(H_z \rightarrow N_z)/R_N(N_z)$. The frequency in the average spectral density, $<J(\omega_H)>$, may be taken equal to $0.87\omega_H$ (Farrow et al., 1995).

In addition to a better sampling of the spectral density function, a comparison of J(0) values at different B_0 strengths provides a means of screening the relaxation data for $R2_{ex}$ contributions. Since $R2_{ex}$ scales as the square of the ω_N Larmor frequency, we can write $R2_{ex} = \Phi\omega_N^2$ (Peng and Wagner, 1995). Φ is then derived from the observed $J(0)_{obs}$ at two B_0 fields ($field_1$ and $field_2$) via the ratio:

$$\Phi = (J(0)_{obs1} - J(0)_{obs2})/(\lambda_1\omega_{N1}^2 - \lambda_2\omega_{N2}^2) \quad (2)$$

λ_1 and λ_2 are scale factors $(3/2)[1/(3d^2+c^2)]$ and are approximately 0.34 and 0.31 ns/rad at 9.4 and 14.1 T, respectively. The true value of J(0), corrected from exchange processes, can therefore be expressed as (Peng and Wagner, 1995):

$$J(0) = J(0)_{obs} - \lambda\omega_N^2\Phi \quad (3)$$

J(0) is field independent and λ depends on ω_N^2 through the CSA factor c^2. It has also been proposed to extract the $R2_{ex}$ value from the linear relation between $2R_N(N_{xy}) - R_N(N_z)$ and ω_{N2}^2 (Habazettl and Wagner, 1995; Vis et al., 1998): this approach yields similar results as those obtained from Equation 2, when using the experimental relaxation rates measured on p13^{MTCP1}.

The model-free approach of Lipari and Szabo (1982) was then used to further describe the mobility in terms of specific types of motion. This formalism makes the assumption that overall and internal motions contribute independently to the reorientational time correlation function of ^{15}N-^{1}H vectors and that internal motions occur on a much faster time scale than the global rotation of the molecule. For an isotropically tumbling protein, one obtains:

$$J(\omega) = \frac{2}{5}\left\{S_f^2\frac{\tau_c}{1+(\omega\tau_c)^2} + (1-S_f^2)\frac{\tau}{1+(\omega\tau)^2}\right\} \quad (4)$$

where τ is the harmonics of the overall and the internal (fast) correlation time which pertains to each residue: $\tau^{-1} = \tau_c^{-1} + \tau_f^{-1}$. Fast internal motions are characterized by the square of a generalised order parameter S_f^2, which describes the relative amplitude of internal motions and ranges from 0 to 1, and an internal correlation time τ_f for the internal motions.

For some of the residues, the simple form of Equation 4 turns out to be insufficient to fit the whole set of experimental data. This occurs when residues exhibit internal motions in a time window close to 1 ns. In this case, the expression for the spectral density function is extended to (Clore et al., 1990b):

$$J(\omega) = \frac{2}{5}\left\{S_f^2S_s^2\frac{\tau_c}{1+(\omega\tau_c)^2} + S_f^2(1-S_s^2)\frac{\tau}{1+(\omega\tau)^2}\right\} \quad (5)$$

with $\tau^{-1} = \tau_c^{-1} + \tau_s^{-1}$, where S_f^2 and S_s^2 are the square of the partial order parameters for fast (picosecond time scale) and slow (τ_s, nanosecond time scale) internal motions, respectively. The square of the generalized order parameter S^2, defined as $S_f^2S_s^2$, is a measure of the total amplitude of the internal motions. Note that S^2 equals S_f^2 in Equation 4. Equation 5 assumes that the contribution of the fastest motion to the spectral density function is negligible.

The values of the motional parameters of the individual residues can be derived from the fit of experimental J(0), J(40 MHz), J(60 MHz), <J(400 MHz)> and <J(600 MHz)> using Equations 4 and 5. An iterative non-linear least-squares algorithm (Press et al., 1986) was employed to further minimize the error function. The 'extended' model was selected if χ^2 was larger than the appropriate critical value (95% confidence interval) and if this more complex model could be statistically justified by a Fischer–Snedecor test (F-test) (Saporta, 1990).

Results

NMR structure refinement and comparison with X-ray structures

In our first model for the 3D solution structure of p13^{MTCP1}, obtained by homonuclear proton 2D NMR methods at 600 MHz (Yang et al., 1998), 87% of the proton resonances were unambiguously assigned. In the present study, all the previously made proton assignments were easily confirmed and extended in the

^{15}N planes of the [^{1}H-^{15}N] 3D NMR experiments at 600 MHz and in the homonuclear 2D NMR experiments at 800 MHz: the backbone and aliphatic side chain ^{1}H, ^{15}N resonance assignments of p13^{MTCP1} at pH 6.5 have been completed, except for the C-terminal Asp107 due to fast exchange with water. The resulting ^{1}H and ^{15}N assignments are available from the authors as Supplementary material.

The substantial increase in NMR restraints (Table 1 and Figure 1a) translates in an approximate twofold decrease in the average rmsd values compared to our previous model, for all structural elements. The excellent convergence of the solution structure modeling calculations is supported by rmsd values generally smaller than the ones calculated from the crystallographic B-factors for the X-ray structure of p13^{MTCP1} (Figure 1b). The main structural motif of p13^{MTCP1} is an orthogonal β-barrel consisting of eight antiparallel β-strands of variable length, with a unique and common topology of this oncoprotein family (Figure 2a). The β-strands are arranged into two very similar up-and-down four-stranded β-meander motifs: motif1, composed of strands A–D, and motif 2, composed of strands E–H. Each motif consists of one short (A–B or E–D) and one long (C–D or G–H) two-stranded β-sheet, which together form an L-shape. The ends of the long β-strand pairs (C–D and G–H) are not involved in the barrel hydrogen bond pattern, but protrude from the core of the molecule, forming two β-pleated loops. The two β-sheet motifs are connected by a long poorly structured loop (segment Gln48-Pro66). In this loop, NOEs of type (i, i+3) were observed in the [^{1}H-^{15}N] 3D-NOESY-HSQC at 600 MHz and the 2D NOESY experiments at 800 MHz for the segment Arg56-Ser63, consistent with the presence of a helical conformation. This helical segment has been reported in the crystal structure of p13^{MTCP1} but was not detected in our previous NMR structure, due to strong overlapping of many proton resonances of residues in this loop. Nevertheless, relatively strong $d_{\alpha N}$ (i, i+1) effects were found concomitantly with d_{NN} (i, i+1) effects, suggesting a conformational equilibrium between the helix and an extended or more flexible conformation within this peptidic segment. Supporting this assumption, the $^{3}J_{NH-H^{\alpha}}$ coupling constants measured for residues Arg56, Leu61 and Thr62 are in the range of 6 to 7 Hz, which significantly deviate from the expected value of 4 Hz in a helix, and those measured for residues His59 and Leu60 are not consistent with a helical structure (9.1 ± 0.2 Hz and 8.0 ± 0.6 Hz, respectively). Finally, the ^{15}N relaxation study indicates that significant exchange processes take place in this peptidic segment (vide infra). A stereodiagram of the superposition of the 20 final structures is shown in Figure 2b. The results of the refinement are provided in Table 1.

The rms deviations between the average NMR and X-ray structures (Figure 2c) testify to their high level of similarity since most of the values are below 1 Å, with global rmsd values of 0.9 Å and 1.43 Å for backbone heavy atoms and side-chain heavy atoms, respectively. The largest differences are found in the loop connecting the two β-strand motifs (segment Gln48-Pro66) and in a turn region for residues Arg94 and Gly95. The loop segment 48–66 is one of the least well-defined regions in the NMR structure, whereas in the X-ray structure the first half of this loop, from residue Gln48 to Ala55, appears well resolved. This difference comes from intermolecular contacts which stabilize the conformation seen in the crystal. The second half of this loop adopts a helical conformation from Arg56 to Ser63 both in the X-ray and in the NMR structure. The large rmsd values seen in this region are due to the global displacement of the helix between the NMR and crystal structure. Indeed, several intermolecular contacts are found in the crystal, in which two helices from different molecules pack together. Similarly, the differences observed in the segment Arg94-Gly95 can be explained by the crystal packing. In other places, discrepancies can be attributed to a lack of resolution in either the NMR or the X-ray structure. Thus, if the poor resolution of the β-turn connecting strands E and F in the NMR structure can explain the increased rmsd value observed for residues Pro73 and Glu74, the lack of resolution in the X-ray structure can be invoked to explain the rmsd value observed for the side-chain of Gln48: the side-chain atoms of this residue are not well defined in the X-ray structure (B-factors ranging from 34.7 Å^2 to 43.4 Å^2), whereas the conformation of this side-chain is perfectly defined in the NMR structure, where Gln48 makes hydrogen bonds with the side-chain of Gln46. Finally, some discrepancies between the NMR and the X-ray structures cannot be explained, neither by crystal packing nor by inadequate resolution, and actually reflect differences between the crystal and the solution structure. Thus, the Trp14 side-chain displays a different orientation in solution than in the crystal, stabilized by a hydrogen bond between the indole Hϵ_1 of the tryptophan and the Sδ atom of the Met68 side-chain. Interestingly, in the p14^{TCL1} structure, the tryptophan side-chain adopts an intermediate confor-

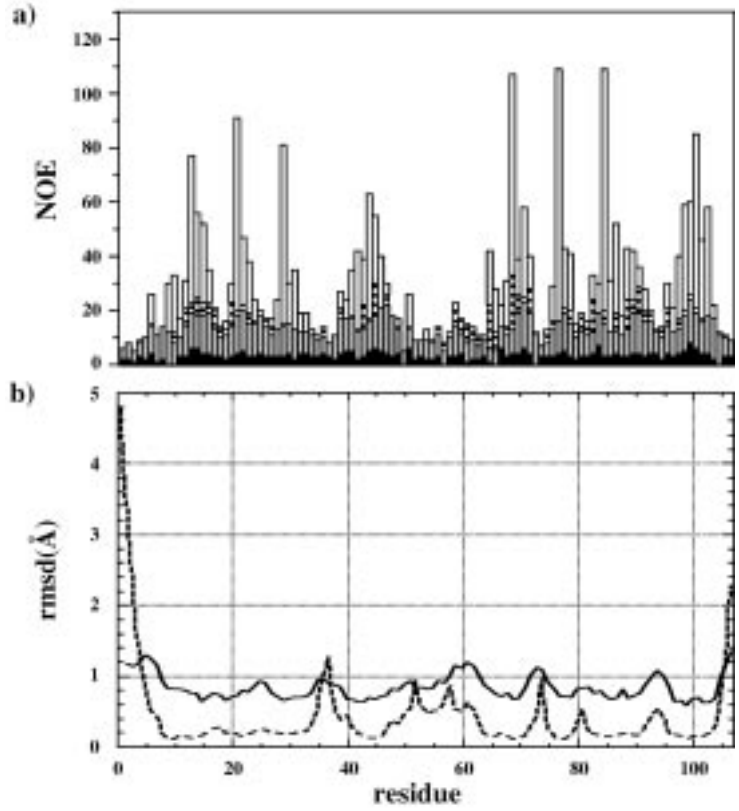

Figure 1. (a) Plot as a function of the amino acid sequence of the number of NOE constraints used in the final structure calculation of the 20 solution structures of p13^{MTCP1}. NOE categories are shown as follows: intraresidue, black; sequential, dark shaded; medium range, light shaded; long range, open. NOEs are counted twice. (b) Plots versus the amino acid sequence of the mean of the rms deviations calculated for the backbone heavy atoms from the 20 NMR structures superimposed over the peptidic segment 9–105 (broken line) and from the X-ray structure (plain line). Rmsd values of the X-ray structure were calculated using the B-factors by applying rmsd $= [(3B/(8\pi^2)]^{-1/2}$ (Blundell and Johnson, 1976).

mation compared to those observed in the X-ray and NMR structures of p13^{MTCP1}, suggesting a kind of flipping motion of this side-chain. The rmsd of 1.8 Å measured for the Arg22 side-chain is probably a consequence of the different orientation of the spacially close side-chain of Trp14.

Similar conclusions can be drawn from the comparison of the solution structure of p13^{MTCP1} and the crystal structure of p14^{TCL1}: most of the differences are dictated by crystal contacts (data not shown). Nevertheless, divergences observed in strand C and in the turn joining strands C and D could be attributed to divergences in the protein sequences rather than to crystal packing. In this region, two insertions in the sequence of p14^{TCL1} (Figure 3a) induce slight conformational differences aimed at preserving the clustering of hydrophobic residues in the β-barrel interior. Thus, a β-bulge is present at the entry of strand C, and, as a consequence, the hydrophobic side chain of Leu37 involved in the bulge is solvent exposed (Figure 3b). For a similar reason, the turn between strands C and D accommodates a surnumeral residue (Gln46). Interestingly, the main dimer contact in the p14^{TCL1} crystal structure is conferred by the antiparallel β-sheet packing of the C-strands (residues 37–41) of the two monomers. It can be postulated that the stable dimeric association of p14^{TCL1} is induced by the different conformation of strand C, as compared to the one observed in the monomeric protein p13^{MTCP1}. Moreover, it is remarkable that most solvent exposed residues in this peptidic segment are hydrophobic in p14^{TCL1}: they form a hydrophobic cluster which stabilizes the dimeric association (Figure 3c). In the structure of p13^{MTCP1}, a different distribution of hydrophobic and hydrophilic residues in this peptidic segment should hamper a hypothetic dimeric associ-

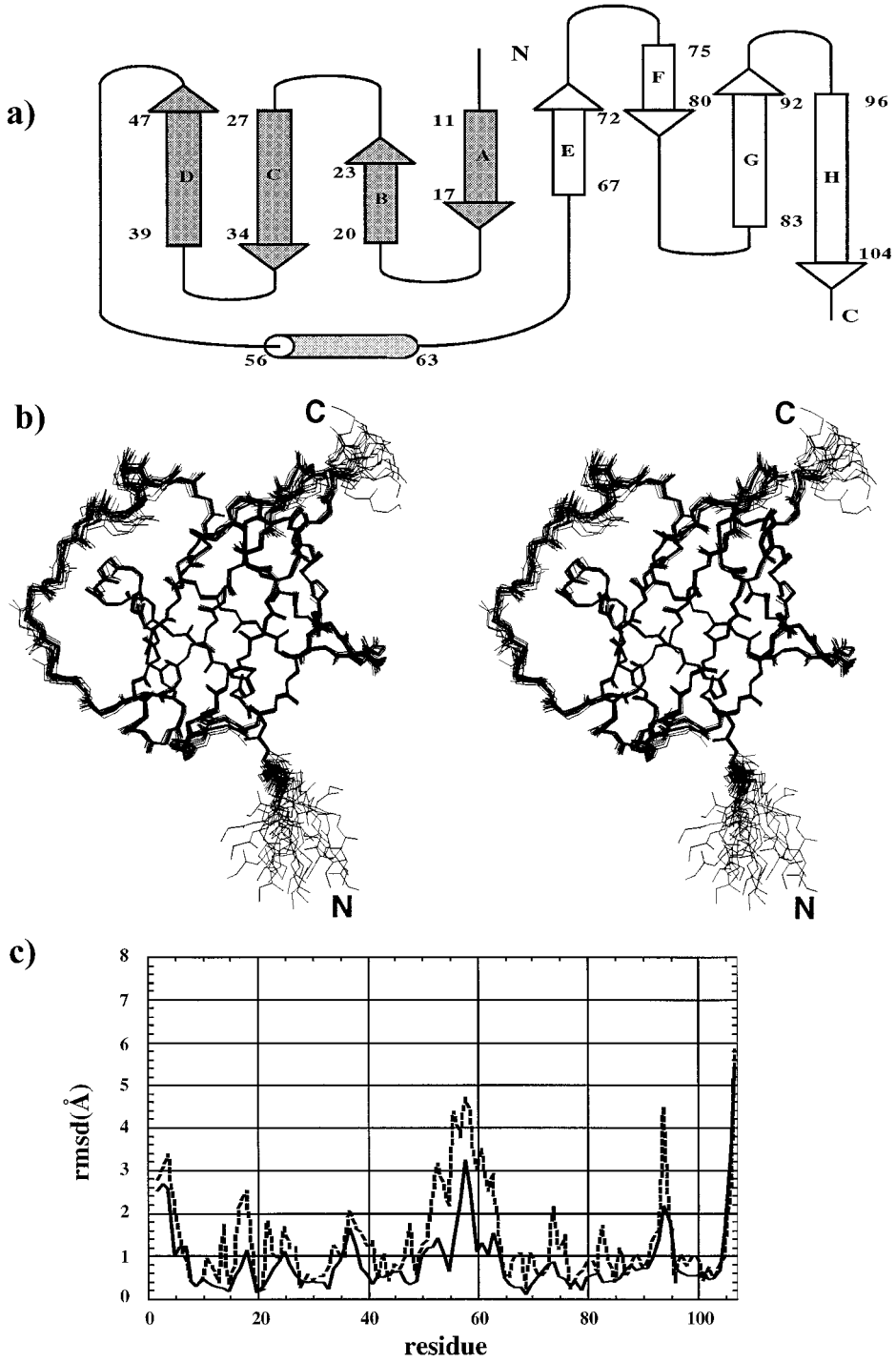

Figure 2. (a) Diagram of the secondary structure of p13^{MTCP1} showing the strands labelled from A to D (gray) and E to H (white), and the helix. (b) Stereodiagram of the 20 final NMR structures of p13^{MTCP1} superimposed on the backbone atoms from residue 6 to the last residue 107. Among 93 'meaningful' residues (i.e., non-glycine, non-proline, and non-terminal residues) of the energy minimized average structure, 77 residues (i.e. 82.8%; 73.3% in our previous model, 85.9% in the crystal structure) fall in the most favored regions of the Ramachandran plot (Ramachandran et al., 1971; Laskowski et al., 1993), 16 residues (i.e. 17.2%; 24.8% in our previous model, 14.1% in the crystal structure) are in the additional allowed regions, and no (2% in our previous model) residue falls in the generously allowed or in the disallowed regions. The coordinates of the solution structure of p13^{MTCP1} have been deposited in the Protein Data Bank (codes: 1QTU (average structure) and 1QTT (20 calculated structures)). (c) Plots versus the amino acid sequence of the average rms deviations of backbone (plain line) and side-chains (broken line) heavy atom coordinates between the average NMR structure and the X-ray structure.

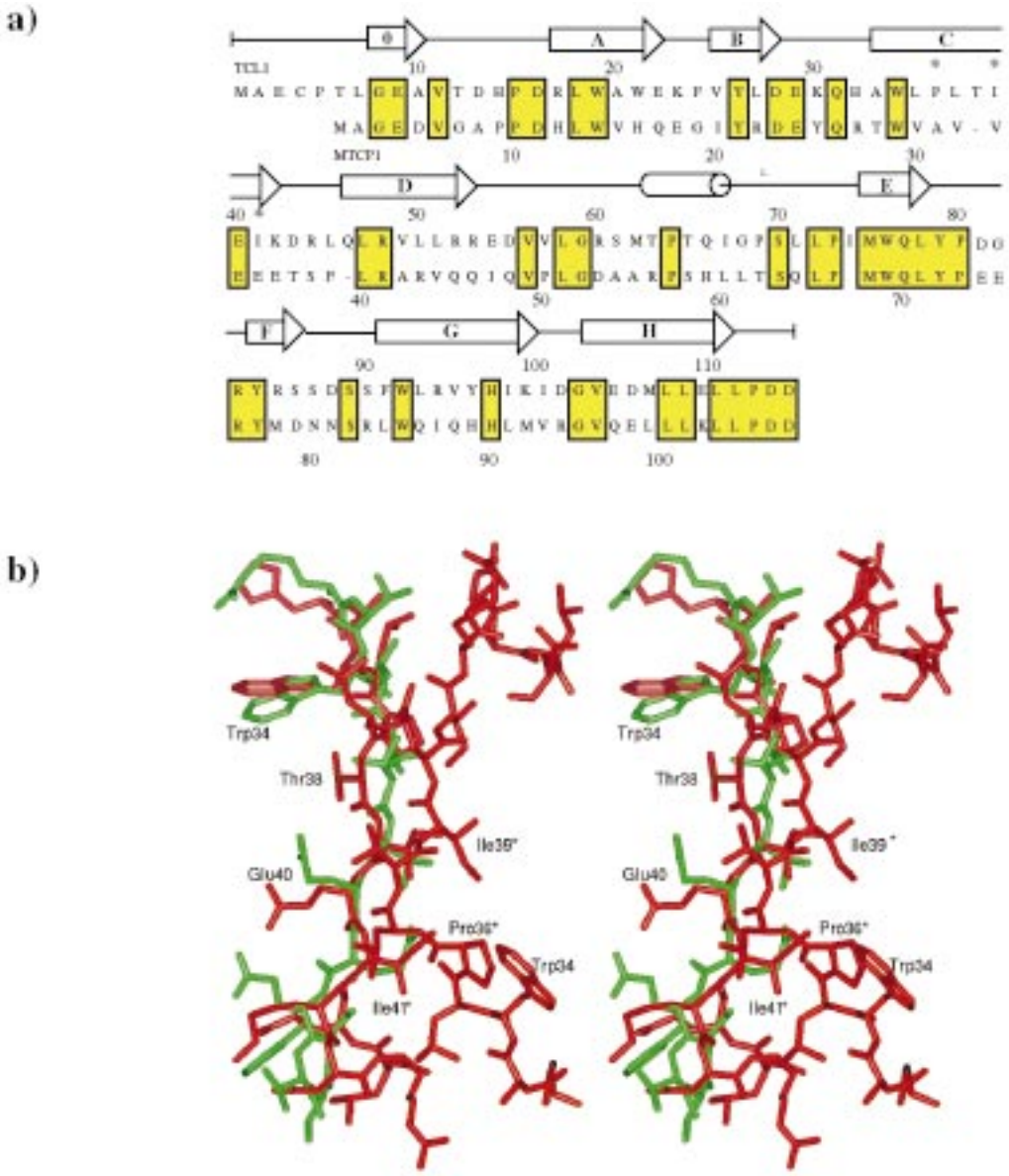

Figure 3. (a) Sequence alignment and secondary structure assignment of p14^{TCL1} (top row) and p13^{MTCP1} (bottom row). Strictly conserved residues are boxed in yellow. The first strand labeled 0 is only present in the crystal structure of p14^{TCL1}. Strand C is involved in the dimerisation contact zone of p14^{TCL1}. The residues directly involved in the dimeric association are labeled with stars. (b) Stereodiagram of the superimposition of the peptidic segment 32–46 (strand C and turn between strands C and D; p14^{TCL1} numbering) in the average NMR structure of p13^{MTCP1} (green) and in the X-ray structure of p14^{TCL1} (red). The symmetry related residues in the dimer are shown for the X-ray structure of p14^{TCL1}. (c) CPK views of the dimerisation surface in p14^{TCL1} (left) and in a hypothetic dimeric model of p13^{MTCP1} (right). Hydrophobic residues are coloured in yellow, polar in orange, negatively charged in red, positively charged in blue, and the backbone atoms in green.

Figure 3. (continued).

ation, due to repulsive interactions between the negatively charged side-chain of Glu40 on each monomer (Figure 3c).

Amide ^{15}N relaxation parameters and spectral function analysis

Spectral density values at 0, 40, 60, 348 and 522 MHz were calculated from the experimental ^{15}N R_1, R_2 and $^{15}N\{^1H\}$NOEs values obtained for 87 of the 100 non-proline residues of p13^{MTCP1} from spectra recorded at 600 MHz and 400 MHz (full list available as Supplementary material) using Equation 1 (Figure 4). The low J(0) values for the terminal residues as well as, to a lesser extent, for the peptidic segments Glu35-Leu40 and Gln48-Leu65 are indicative of an increased flexibility. The segment Glu35-Leu40 belongs to the first four-stranded antiparallel β-sheet motif (long strands C and D) but does not participate in the β-barrel: it is solvent-exposed and forms one of the structured β-pleated loops which protrudes out of the β-barrel. The segment Gln48-Leu65 forms the long poorly structured loop which joins the two β-meanders, comprising the helical region. In these regions, reduced values of J(0) for flexible residues with respect to the rigid part of the protein (the β-barrel) are compensated for by high values of $<J(\omega_H)>$. This supports the fact that the higher values of rmsd observed in this less well-defined region are due to intrinsic flexibility rather than to a lack of structural data. Low $<J(\omega_H)>$ values for the rest of the protein indicate restricted flexibility on fast time scales. At 40 MHz, J(ω) values exhibit a pattern similar to that observed for J(0): a decrease is observed for NH vectors located on the loop and, to a lesser extent, for NH vectors located on the segment Glu35-Leu40. At 60 MHz, the distribution of J(ω) as a function of residue number is almost flat, indicating proximity to the isobestic frequency, where the contribution of J(ω) is independent of the internal mobility.

The J(0) values reported in Figure 4 have been corrected for exchange contributions on the μs to ms time scale (see Materials and methods). For almost all backbone NH bonds, significant exchange contributions are observed with Φ ranging from approximately 0.5×10^{-17} s/rad to 1.5×10^{-17} s/rad (Figure 5b). This suggests the presence of widespread exchange processes for p13^{MTCP1}. However, the uncertainties in the values of Φ are rather high, such that the plenitude of small Φ values could either be indicative of an unidentified global exchange process, for example due to protein aggregation, or reflect an artifact from a presently unaccounted for field dependence in the relaxation rates. Nevertheless, significant increases in Φ values (up to 6×10^{-17} s/rad) are seen for different peptidic segments in the protein. Thus, most of the NH

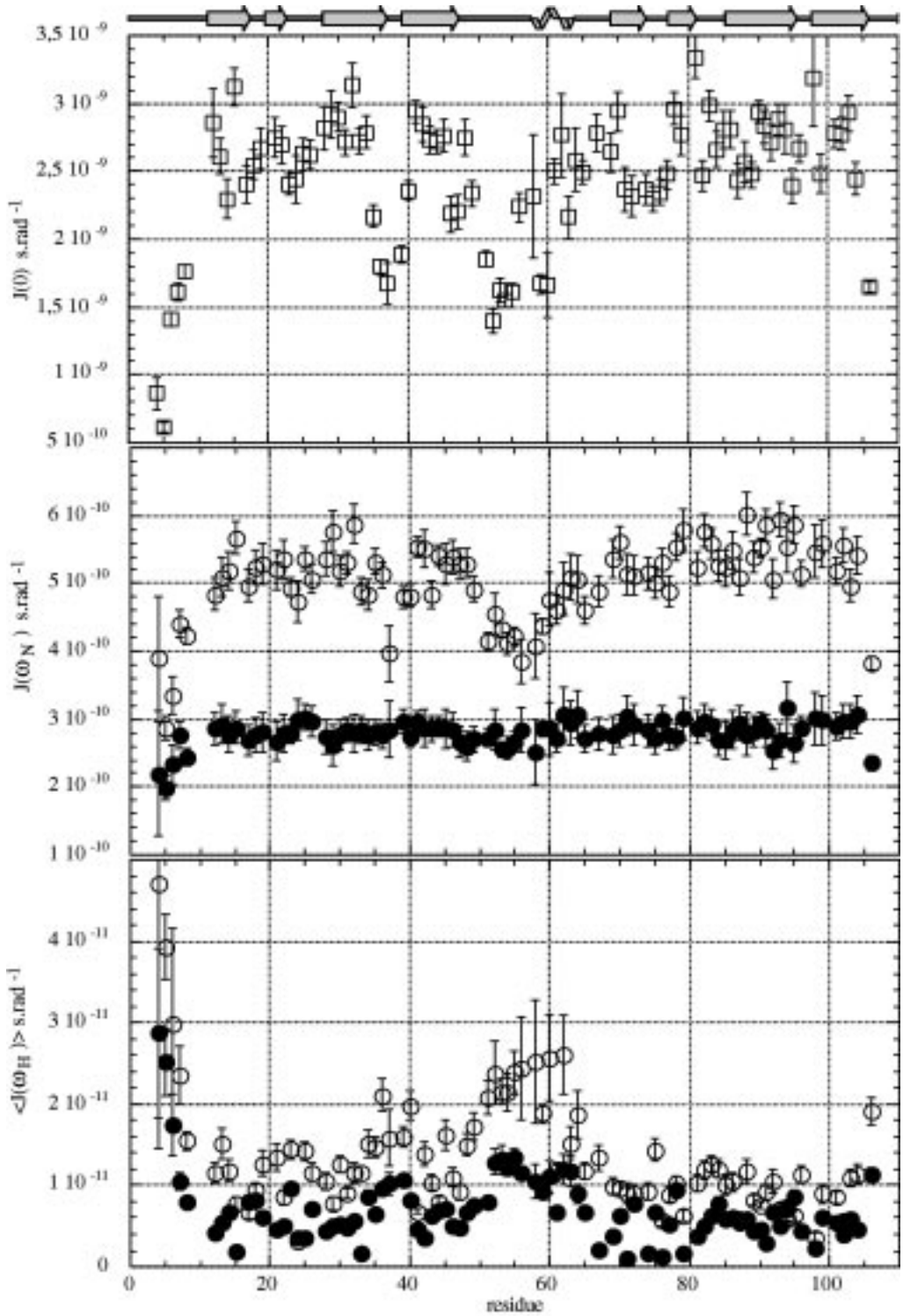

Figure 4. Plots of the reduced spectral density at (from top to bottom) 0 Hz, ω_N (40 and 60 MHz), $<\omega_H>$ (348 and 522 MHz) as a function of the residue number for p13^{MTCP1} at 30 °C. The values displayed were calculated according to Equation 1 (Materials and methods). J(0) values were corrected from exchange processes (see Materials and methods). The secondary structure elements are schematized above the data.

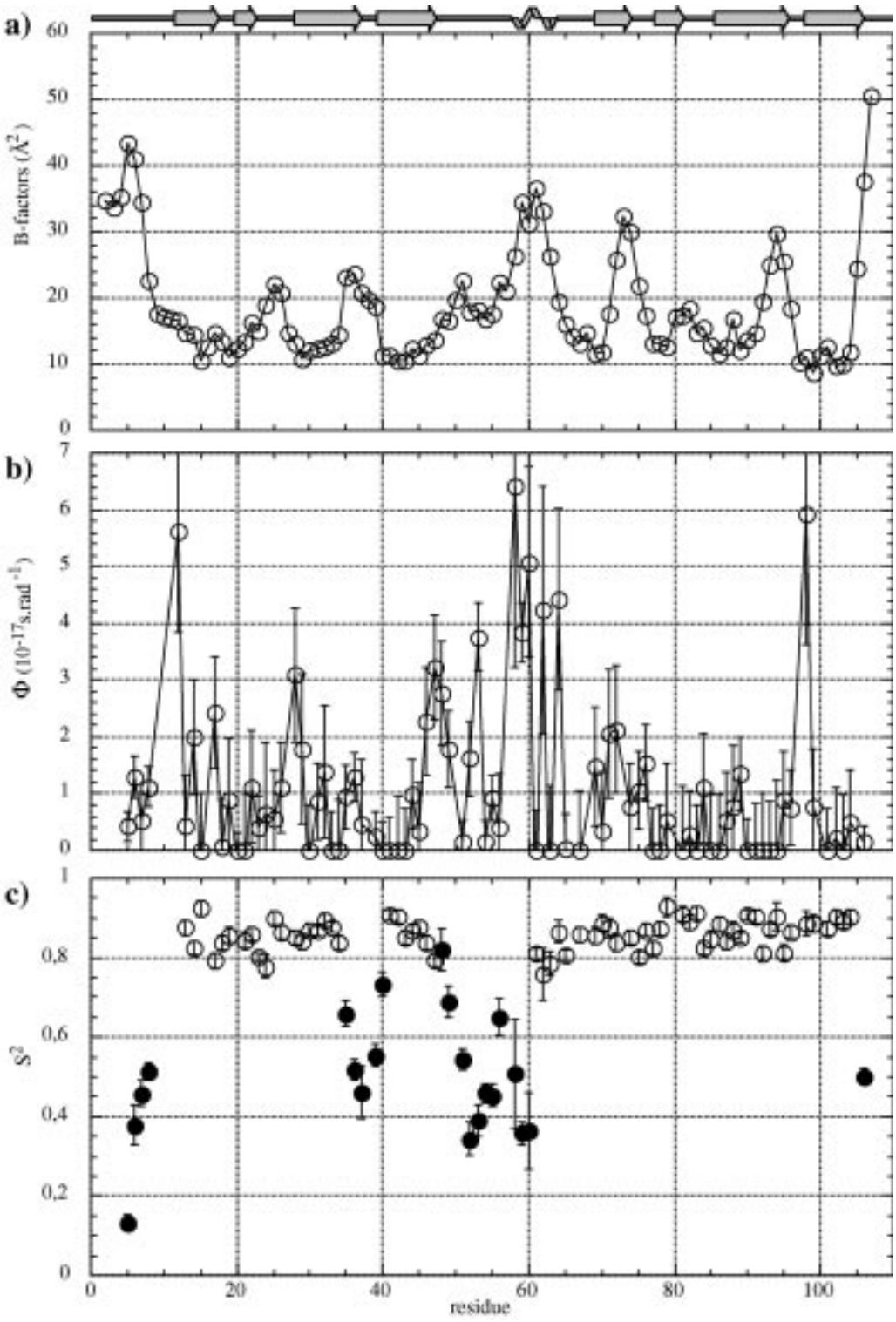

Figure 5. Dynamical parameters obtained for p13^{MTCP1}. (a) X-ray B-factors versus protein sequence. (b) Exchange parameter ϕ versus protein sequence. The ϕ values were obtained according to Equation 2 (Materials and methods). (c) Generalized order parameters S^2 obtained from the model-free analysis. The two-parameter spectral density function (Equation 4) has been used except when S^2 are plotted as filled circles: for these residues, the extended Lipari–Szabo formalism has been used (Equation 5) and the value of the order parameter is given as $S_f^2.S_s^2$. Blanks indicate prolines or NH bonds which were excluded from the analysis.The secondary structure elements are schematized above the data.

Table 1. Experimental constraints and refinement statistics of the 20 conformers representing the solution structure of p13^{MTCP1} before and after restrained energy minimization

Distance constraints		
Total	1773	
Intraresidue	347	
Sequential	527	
Medium range ($\|i-j\| \leq 4$)	158	
Long range ($\|i-j\| > 4$)	741	
Dihedral angle restraints		
Φ	36	
χ_1	35	
χ_2	9	
	20 conformers (DYANA)	Average structure (AMBER)
Target function (Å^2)	2.28 ± 0.16	
Upper limit violations:		
Number > 0.2 Å	1 ± 1	0
Sum of violations (Å)	17.2 ± 0.5	7.3
Maximum violation (Å)	0.22 ± 0.04	0.19
Dihedral angle violations:		
Number $> 5°$	0	
Sum of violations	0.2	
Maximum violation	0.06 ± 0.01	
van der Waals violations:		
Number > 0.2 Å	0	
Sum of violations (Å)	6.2 ± 0.5	
Maximum violation (Å)	0.17 ± 0.04	
AMBER energies (kcal mol^{-1})		
Bond energy		36.3
Valence angle energy		303.6
van der Waals energy		−884.9
Electrostatic energy		−3118.5
Constraint energy		39.4
Total non-bonding energy		−963.1
Total energy		−1925.5

vectors located on the loop joining the two β-meander motifs (Gln48-Leu65) exhibit high Φ values, with a peak centered on the helical segment Arg56-Ser63. The presence of such intensive exchange processes strongly supports the conclusions previously drawn from the structural data, suggesting a possible equilibrium between helical and random conformations for residues located in this peptidic segment. Exchange processes are possibly reinforced by isomerization of the proline residue (Pro57) in the N-terminal end of the helical segment. Similar increases are seen on two peptidic segments, centered on residues Pro10 and Glu98. These segments are both located at the junction of the two β-meanders forming the β-barrel, and residue Glu98 ends the second β-pleated loop, suggesting that this loop exhibits very slow hinge-motions on the μs to ms time scale. Weaker contributions of exchange processes are also seen centered on or in the vicinity of aromatic residues: Arg27 (sequential to Tyr26) and Tyr72. These residues are involved in β-bulges in the non-canonic β-hairpin joining strands B–C and E–F, respectively. Due to their ring-current,

the motion of aromatic side-chains creates strong chemical-shift gradients on the neighbouring residues, leading to very efficient relaxation pathways. Such processes are not clearly seen in the other turns, probably due to the lack of aromatic residues in their sequence.

The mapping of spectral densities $J(\omega)$ for each backbone NH bond provides the intrinsic dynamic information from the relaxation data – without any assumption for the motional model – upon which a variety of motional models may be evaluated. Since both values of $J(\omega_N)$ and $J(\omega_H)$ decrease for almost all NH vectors with increasing frequencies ω_N and ω_H, respectively, the description of the spectral densities as sums of Lorentzians appears qualitatively reasonable for $p13^{MTCP1}$. Adequate fits of $J(\omega)$ are therefore expected using the model-free formalism proposed by Lipari and Szabo (1982). The combination of relaxation data sets from two different magnetic fields resulted in five independent values of the spectral density function per NH bond, while a maximum of only three parameters using Equation 5 ('extended' Lipari–Szabo model (Clore et al., 1990b)) is required to model $J(\omega)$, giving a substantially high number of degrees of freedom. We thus tentatively use the 'non-simplified extended' Lipari-Szabo model (Clore et al., 1990b), introducing τ_f as a fourth additional parameter for the fit, but this procedure did not give significant improvements. On the other hand, the ratio of the principal components of the average inertia tensor for the backbone atom on the average structure of $p13^{MTCP1}$ was determined to be (1.9: 1.7: 1.2). These numbers suggest that the overall rotation of the protein is expected to have only a small degree of anisotropy that may not have a strong influence, at least on the order parameter values (Tjandra et al., 1995). Thus, we do not make any attempt to introduce this contribution in the motional model.

The global value of the overall rotational correlation time τ_c was taken as the average of the values obtained independently for all residues which were well parametrized (low χ^2) by the 'simple' Lipari–Szabo formalism (Equation 4) and showed order parameters higher than 0.70. This procedure leads to a correlation time equal to 7.69 ± 0.05 ns. Once the overall tumbling time τ_c has been determined, local model-free parameters were obtained by using either the 'simple' or the 'extended' (Equation 5) Lipari–Szabo formalisms. The internal dynamics of most backbone NH bonds located in the β-barrel are satisfactorily parametrized using Equation 4. For the N- and C-terminal residues, the use of Equation 5 is required. The 'extended' model was also necessary to correctly describe the dynamics of the NH vectors located in the solvent-exposed Glu35-Leu40 peptidic segment and in the long flexible loop, including residues in the N-terminal turns of the helix (Arg56, Ser58, His59 and Leu60). The use of the 'extended' model was fully justified by the statistics, and, supporting this choice, reasonable values of τ_s (0.5–1.5 ns) were observed while it brought undeniable improvements of the fit.

Figure 5 shows a comparison between the B-factor obtained from the X-ray data of $p13^{MTCP1}$ and the generalized order parameters S^2 obtained from the relaxation study, as a function of the residue number. Except for the few exceptions further mentioned, the crystallographic B-factors obtained for $p14^{TCL1}$ parallel those reported for $p13^{MTCP1}$ (data not shown). Thus, these two proteins have not only a similar structure, but also a very similar dynamic behavior in the crystal. The lowest B-factor values are observed for residues in the β-barrel, except for those located in the solvent-exposed segments of the two β-pleated loops (Val32-Phe39 and His89-Val96) or in the turns joining strands B–C (Asp23-Arg27) and E–F (Tyr72-Arg76). Such a flexibility is not observed for the two other turns (joining A–B and F–G), located on the opposite face of the β-barrel. In solution, as judged by S^2 values ranging between 0.8 and 0.9, residues belonging to the β-barrel seem to experience extremely restricted mobility. Only residues located in the solvent-exposed segment Glu35-Leu40 show significantly lower S^2 values, with an additional contribution of an internal slow motion on the ns time scale to the NH dynamics. Interestingly, and contrary to what is observed in the crystal, low S^2 values are not observed, either in the peptidic segment His89-Val96, symmetrically disposed on the second β-pleated loop, or for the residues located in turns. Nevertheless, different motions are known to contribute to the value of X-ray isotropic B-factors: thermal fluctuations, static and dynamic conformational disorder (molecules existing in different conformations in the crystal), and lattice disorder (crystal heterogeneity). Thus, B-factors reflect protein mobility on two distinct time scales: 10^{-15} to 10^{-11}s (fast thermal fluctuations) and 10^{-9} to 10^{-3} s (conformational changes). Rather than a crystal artefact, we believe that the increased B-factor values seen for residues in the peptidic segment His89-Val96 are consistent with the existence of a possible slow hinge-motion of this loop. In solution, this motion was suggested by the analysis of transverse relaxation

rates at two B_0 fields which demonstrated that exchange processes took place in the same area of the protein, centered around residue Glu98. Similarly, the slight increases in Φ values observed for residues in the segments Gln26-Thr28 and Trp69-Tyr72 suggest that slow exchange motions take place in the turns joining the strands B–C and E–F. In solution, the long loop joining the two β-meander motifs exhibits very complex motions. An additional contribution of an internal slow motion on the ns time scale is needed to describe the motion of the residues located in the segment Val49-Leu60, spanning the unstructured part of the loop and the first half of the helical segment. In this peptidic segment, S^2 parameters drop from about 0.8 (Val49) to 0.35 for Gly52, in the central part of the unstructured loop, and increase again up to residue Arg56, at the entry of the helix, indicating a relation between the decrease of the motion restriction and the remoteness of the considered residue from the structured core of the protein. Then, S^2 parameters drop again until residue Leu 60, in the centre of the helical segment, whereas fast motions – on the ps time scale – in the second half of the helix appear as restricted as in the β-barrel. In addition, this loop undergoes very slow motions on the μs to ms time scale, as indicated by the Φ values measured in this segment. As previously quoted, exchange processes appear to affect predominantly residues in the helical segment. The high B-factor values observed in the helix indicate that this segment also exhibits an enhanced mobility in the crystal of $p13^{MTCP1}$ but, contrary to what is observed in solution, the unstructured part of the loop (residues Gln48-Arg56) shows only a slight increase in B-factors. This different behavior between the solution and the crystal could be attributed to the close packing of this loop in the crystal structure. Interestingly, this loop shows high B-factor values in the crystal of $p14^{TCL1}$ (data not shown), its dynamics being less affected by the packing of the dimer. Finally, the N- and C-terminal ends of the protein appear very flexible in both the solution and the crystal, even though the very first residues show slightly lower B-factors, certainly due to the presence of intermolecular interactions in the crystal structure.

Discussion

Owing to the enhancement of the spectral resolution brought either by the 3D [^{15}N,^{1}H] NMR heteronuclear experiments recorded on the ^{15}N-labeled protein or by the very high resolution (800 MHz) 2D NMR homonuclear experiments, the solution structure of $p13^{MTCP1}$ has been considerably improved with regard to our previous model. This improvement does not limit itself to the finding of an helical segment in the long flexible loop joining the two β-motifs, as was already observed in the crystal structure, but it also allows a better resolution of the β-barrel itself, as indicated by the very low rmsd values. Thus, the final structures conform better to the stereochemical standards and an accurate comparison can be done with the crystal structure. $P13^{MTCP1}$ is a compact molecule belonging to the β class of proteins with 50% of its residues arranged into β-strands. Not surprisingly, the structure in solution is virtually identical to that found in the crystal, with rmsd values of 0.9 Å and 1.43 Å for backbone atoms and all heavy atoms, respectively. Most of the differences have been related to the packing of the protein in the crystal. Indeed, the stability of such a structural motif is subject to severe geometric rules (Murzin, 1994a,b), such that minimal variations are expected between the crystal and the solution structure. Interestingly, although the two structures are roughly similar everywhere else, a different conformation is observed for strand C in the structure of $p14^{TCL1}$, due to residue insertion, which has been correlated to the formation of a stable dimer both in solution and in the crystal.

In addition to a similar structure, $p13^{MTCP1}$ has also very similar dynamic behavior in solution and in the crystal, but the ^{15}N relaxation data analysis brings out details on the time scales of the motions which are not attainable from the inspection of the B-factors. Thus, the high B-factor values observed for residues in the two β-pleated loops emerging from the barrel indicate an increased flexibility in the crystal. In solution, these loops also appear flexible, but motions on a very different time scale are involved in their intrinsic dynamics. Additional sub-nanosecond motions are detected in the loop emerging from the C–D β-sheet, and a significant decrease of the generalized order parameter indicates little restriction for these internal motions. On the opposite face of the barrel, the loop supported by the G-H β-sheet undergoes a slow hinge-motion, on the μs to ms time scale. The consistence of the data with the Lipari–Szabo model indicates that internal motions in this loop are fast, on the ps time scale, and highly restricted, as supported by S^2 values close to 1. Similarly, the relaxation analysis shows that the dynamics of the long flexible loop joining the two β-motifs is very complex. In addition to nearly unhin-

dered sub-nanosecond motions, strong conformational exchange contributions participate to the movement of this loop in solution. These exchange contributions are especially strong in the helical segment, which also exhibits high B-factor values in the crystal.

The two β-pleated loops delimitate a large concave surface on the exterior of the β-barrel, with a striking richness in solvent-exposed hydrophobic residues (45% of the solvent-exposed residues), which might be a possible interaction surface. This has been postulated in our previous work on the basis of the high sequence homology between p13^{MTCP1} and p14^{TCL1}: among 22 solvent-exposed residues on this surface on p13^{MTCP1}, 14 are conserved in p14^{TCL1}, including all the hydrophobic residues. The conformational flexibility observed in the loops may promote the docking process by thermally induced motions. This surface is considerably enlarged in the dimer of p14^{TCL1}. NMR diffusion experiments (unpublished results) have shown that the dimer is stable in solution: it possibly constitutes the physiological active form of the protein. If the proteins of this family are targeted toward similar molecular partner(s), this raises the question of a possible dimerisation of p13^{MTCP1} under physiological conditions or when complexed to its partner. Note that the large insertion (17 residues) at the exit of strand C in p14^{TCL1b} precludes any safe conclusion about the possible dimerisation of this new member of the p13^{MTCP1} oncogenic protein family. With only 33% identity, the long flexible loop has been previously discarded as being involved in an interaction common to p13^{MTCP1} and p14^{TCL1}. Nevertheless, it is rather disconcerting that a similar region of this loop, without any sequence homology, is involved in a similar helical structure in the two proteins. Possibly, this region could play a similar role in the function of the proteins: the different amino acid composition might bring some specificity to the interaction.

Without any information on the molecular partner(s) of these oncogenic proteins, any proposal of a putative binding site or mode of action remains very speculative. But we think that the proposal of a binding site on the surface of the barrel is more realistic than the role of transport proteins suggested by Fu et al. (1998) or Pekarski et al. (1999) from a superficial resemblance with the structure of proteins in the lipocalin protein family (Banaszak et al., 1994). Beyond the fact that the β-barrel found in p13^{MTCP1} (or p14^{TCL1}) adopts a different topology, geometrical considerations about this barrel demonstrate that these oncogenes are *not* related to this protein family. Indeed, the β-barrel found in p13^{MTCP1} belongs to the category 'filled barrel' (Murzin, 1994a,b), with an optimal and dense packing of the hydrophobic side-chains within the barrel. Since there is no cavity in the inside of such a barrel, there is no way for the binding of, even a small, hydrophobic ligand. The high conservation of the amino acids involved in the β-barrels of p13^{MTCP1} and p14^{TCL1} is presumably only due to the presence of this common scaffold: these residues, which contribute to the stability of the β-barrel, have been selected through evolution in addition to those that are responsible for the specific (unknown) function.

Acknowledgements

This work was supported by grants from the Ligue Nationale contre le Cancer and from the Association pour la Recherche sur le Cancer. The authors are indebted to Heinz Rüterjans for giving us access to the 800 MHz DRX800 Bruker spectrometer through the European Large Scale NMR Facility in Frankfurt, and to Frank Löhr for his assistance on this machine. The authors thank Marie-Paule Strub for her help in protein expression, Marie-Hélène Deméné for helpful discussions about statistics and Cathy Royer for critical reading of the manuscript.

Note added in proof

During the reviewing of this manuscript, a report appeared in the literature (Pekarski et al., March 2000) presenting evidence that p14^{TCL1} interacts with the pleckstrin homology domain of the proteine kinase Akt1.

References

Abragam, A. (1961) *Principles of Nuclear Magnetism*, Oxford Science Publication, Clarendon Press, Oxford.

Banaszak, L., Winter, N., Xu, Z., Bernlohr, D.A., Cowan, S. and Jones, T.A. (1994) *Adv. Protein Chem.*, **45**, 89–151.

Barthe, P., Chiche, L., Declerck, N., Delsuc, M.A., Lefèvre, J.F., Malliavin, T., Mispelter, J., Stern, M.-H., Lhoste, J.M. and Roumestand, C. (1999) *J. Biomol. NMR*, **15**, 271–288.

Bax, A., Ikura, M., Kay, L.E., Torchia, D.A. and Tschudin, R. (1990) *J. Magn. Reson.*, **86**, 304–318.

Billeter, M., Neri, D., Otting, G., Qian, Y.-Q. and Wüthrich, K. (1992) *J. Biomol. NMR*, **2**, 257–274.

Blundell, T.L. and Johnson, L.N. (1976) *Protein Crystallography*, Academic Press Inc., London.

Clore, G.M., Szabo, A., Bax, A., Kay, L.E., Driscoll, P.C., Wingfield, P.T. and Gronenborn, A.M. (1990a) *J. Am. Chem. Soc.*, **112**, 4989–4991.
Clore, G.M., Driscoll, P.C., Wingfield, P.T. and Gronenborn, A.M. (1990b) *Biochemistry*, **29**, 7387–7401.
Cornell, W.D., Cieplak, P., Bayly, C.I., Gould, I.R., Merz, K.M. Jr, Ferguson, D.M., Spellmeyer, D.C., Fox, T., Caldwell, J.W. and Kollman, P.A. (1995) *J. Am. Chem. Soc.*, **117**, 5179–5197.
Croce, C.M. (1987) *Cell*, **49**, 155–156.
Farrow, N.A., Zhang, O., Szabo, A., Torchia, D.A. and Kay, L.E. (1995) *J. Biomol. NMR*, **6**, 153–162.
Fesik, S.W. and Zuiderweg, E.R.P. (1988) *J. Magn. Reson.*, **78**, 588–593.
Fisch, P., Forster, A., Sherrington, P.D., Dyer, M.J. and Rabbitts, T.H. (1993) *Oncogene*, **8**, 3271–3276.
Fu, T.-B., Virgilio, L., Narducci, M.G., Facchiano, A., Russo, G. and Croce, C.M. (1994) *Cancer Res.*, **54**, 6297–6301.
Fu, Z.-Q., Du Bois, G.C., Song, S.P., Kulikovskaya, I., Virgilio, L., Rothstein, J.L., Croce, C.M., Weber, I.T. and Harrison, R.W. (1998) *Proc. Natl. Acad. Sci. USA*, **95**, 3413–3418.
Güntert, P. and Wüthrich, K. (1991) *J. Biomol. NMR*, **1**, 447–456.
Güntert, P., Mumenthaler, C. and Wüthrich, K. (1997) *J. Mol. Biol.*, **273**, 283–298.
Habazettl, J. and Wagner, G. (1995) *J. Magn. Reson.*, **B109**, 100–104.
Hiyama, Y., Niu, C.H., Silverton, J.V., Bavoso, A. and Torchia, D.A. (1988) *J. Am. Chem. Soc.*, **110**, 2378–2383.
Hoh, F., Yang, Y.-S., Guignard, L., Padilla, A., Stern, M.H., Lhoste, J.M. and van Tilbeurgh, H. (1998) *Structure*, **6**, 147–155.
Hyberts, S.G., Märki, W. and Wagner, G. (1987) *Eur. J. Biochem.*, **164**, 625–635.
Ishima, R. and Nagayama, K. (1995a) *Biochemistry*, **34**, 3162–3171.
Ishima, R. and Nagayama, K. (1995b) *J. Magn. Reson.*, **B108**, 73–76.
Jeener, J., Meier, B.H., Bachman, P. and Ernst, R.R. (1979) *J. Chem. Phys.*, **71**, 4546–4553.
Kadkhodaei, M., Hwang, T.-L., Tang, J. and Shaka, A.J. (1993) *J. Magn. Reson.*, **A105**, 104–107.
Kay, L.E., Torchia, D.A. and Bax, A. (1989) *Biochemistry*, **28**, 8972–8979.
Kay, L.E., Nicholson, L.K., Delaglio, F., Bax, A. and Torchia, D.A. (1992) *J. Magn. Reson.*, **97**, 359–375.
Laskowski, R.A., MacArthur, M.W., Moss, D.S. and Thornton, J.M. (1993) *J. Appl. Crystallogr.*, **26**, 283–291.
Lefèvre, J.-F., Dayie, K.T., Peng, J.W. and Wagner, G. (1996) *Biochemistry*, **35**, 2674–2686.
Lipari, G. and Szabo, A. (1982) *J. Am. Chem. Soc.*, **104**, 4546–4559.
Madani, A., Soulier, J., Schmid, M., Plichtova, R., Lermé, F., Gateau-Roesch, O., Garnier, J.P., Pla, M., Sigaux, F. and Stern, M.-H. (1995) *Oncogene*, **10**, 2259–2262.
Madani, A., Choukroun, V., Soulier, J., Cacheux, V., Claisse, J.F., Valensi, F., Daliphard, S., Cazin, B., Levy, V., Leblond, V., Daniel, M.T., Sigaux, F. and Stern, M.H. (1996) *Blood*, **87**, 1923–1927.
Marion, D., Driscoll, P.C., Kay, L.E., Wingfield, P.T., Bax, A., Gronenborn, A.M. and Clore, G.M. (1989a) *Biochemistry*, **28**, 6150–6156.
Marion, D., Ikura, M., Tschudin, R. and Bax, A. (1989b) *J. Magn. Reson.*, **85**, 393–399.
Murzin, A.G., Lesk, A.M. and Chothia, C. (1994a) *J. Mol. Biol.*, **236**, 1369–1381.
Murzin, A.G., Lesk, A.M. and Chothia, C. (1994b) *J. Mol. Biol.*, **236**, 1382–1400.
Narducci, M.G., Virgilio, L., Isobe, M., Stoppacciaro, A., Elli, R., Fiorilli, M., Carbonari, M., Antonelli, A., Chessa, L., Croce, C.M. and Russo, G. (1995) *Blood*, **86**, 2358–2364.
Neri, D., Otting, G. and Wüthrich, K. (1990) *J. Am. Chem. Soc.*, **112**, 3663–3665.
Pearlman, D.A., Case, D.A., Caldwell, J.W., Ross, W.S., Cheatham III, T.E., Fergusson, D.M., Seibel, G.L., Chandra Singh, U., Weiner, P.K. and Kollman, P.A. (1995) AMBER 4.1, University of California, San Francisco, CA.
Pekarski, Y., Hallas, C., Isobe, M., Russo, G. and Croce, C.M. (1999) *Proc. Natl. Acad. Sci. USA*, **96**, 2949–2951.
Pekarski, Y., Koval, A., Hallas, C., Bichi, R., Tresini, M., Malstrom, S., Russo, G., Tsichlis, P. and Croce, C.M. (2000) *Proc. Natl. Acad. Sci. USA*, **97**, 3028–3033.
Peng, J.W. and Wagner, G. (1992a) *Biochemistry*, **31**, 8571–8586.
Peng, J.W. and Wagner, G. (1992b) *J. Magn. Reson.*, **98**, 308–332.
Peng, J.W. and Wagner, G. (1995) *Biochemistry*, **34**, 16733–16752.
Piotto, M., Saudek, V. and Sklenar, V. (1992) *J. Biomol. NMR*, **2**, 661–665.
Pons, J.L., Malliavin, T.E. and Delsuc, M.A. (1996) *J. Biomol. NMR*, **8**, 445–452.
Press, W.H., Flannery, B.P., Teukolsky, S.A. and Vetterling, W.T. (1986) *Numerical Recipes*, Cambridge University Press, Cambridge.
Ramachandran, G.N., Chandrasekaran, R. and Kopple, K.D. (1971) *Biopolymers*, **10**, 2113–2131.
Rance, M. (1987) *J. Magn. Reson.*, **74**, 557–564.
Rance, M., Sørensen, O.W., Bodenhausen, G., Wagner, G., Ernst, R.R. and Wüthrich, K. (1983) *Biochem. Biophys. Res. Commun.*, **117**, 479–495.
Santoro, J., Bruix, M. and Rico, M. (1996) *Thirteenth European Experimental NMR Conference*, May 19–24, Paris.
Saporta, G. (1990) *Probabilités, Analyse des Données et Statistique*, Edition Technip, Paris.
Shaka, A.J., Keeler, J. and Freeman, R. (1983) *J. Magn. Reson.*, **53**, 313–340.
Skelton, N.J., Palmer, III, A.G., Akke, M., Kördel, J., Rance, M. and Chazin, W.J. (1993) *J. Magn. Reson.*, **B102**, 253–264.
Sklenar, V. (1995) *J. Magn. Reson.*, **A114**, 132–135.
Soulier, J., Madani, A., Cacheux, V., Rosenzwajg, M., Sigaux, F. and Stern, M.-H. (1994) *Oncogene*, **9**, 3565–3570.
Stern, M.H., Soulier, J., Rosenzwajg, M., Nakahara, K., Canki-Klain, N., Aurias, A., Sigaux, F. and Kirsch, I.R. (1993) *Oncogene*, **8**, 2475–2483.
Thick, J., Metcalfe, J.A., Mak, Y.-F., Beatty, D., Minegishi, M., Dyer, M.J.S., Lucas, G. and Taylor, A.M.R. (1996) *Oncogene*, **12**, 379–386.
Tjandra, N., Feller, S.E., Pastor, R.W. and Bax, A. (1995) *J. Am. Chem. Soc.*, **117**, 12562–12566.
Virgilio, L., Isobe, M., Narducci, M.G., Carotenuto, P., Camerini, B., Kurosawa, N., Abbas-Ar-Rushdi, Croce, C.M. and Russo, G. (1993) *Proc. Natl. Acad. Sci. USA*, **90**, 9275–9279.
Vis, H., Vorgias, C.E., Wilson, K.S., Kaptein, R. and Boelens, R. (1998) *J. Biomol. NMR*, **11**, 265–277.
Yang, Y.-S., Guignard, L., Padilla, A., Hoh, F., Strub, M.P., Stern, M.-H., Lhoste, J.M. and Roumestand, C. (1998) *J. Biomol. NMR*, **11**, 337–354.